

# Making EfficientNet More Efficient: Exploring Batch-Independent Normalization, Group Convolutions and Reduced Resolution Training

Dominic Masters<sup>1</sup> Antoine Labatie<sup>2</sup> Zach Eaton-Rosen<sup>2</sup> Carlo Luschi<sup>1</sup>

## Abstract

Much recent research has been dedicated to improving the efficiency of training and inference for image classification. This effort has commonly focused on explicitly improving *theoretical efficiency*, often measured as ImageNet validation accuracy per FLOP. These theoretical savings have, however, proven challenging to achieve in practice, particularly on high-performance training accelerators.

In this work, we focus on improving the *practical efficiency* of the state-of-the-art EfficientNet models on a new class of accelerator, the Graphcore IPU. We do this by extending this family of models in the following ways: (i) generalising depthwise convolutions to group convolutions; (ii) adding proxy-normalized activations to match batch normalization performance with batch-independent statistics; (iii) reducing compute by lowering the training resolution and inexpensively fine-tuning at higher resolution. We find that these three methods improve the practical efficiency for both training and inference. Our code will be made available online.

## 1. Introduction

Making computer vision models more *efficient* would allow them to exceed the performance of current models given any specified constraints, including: final accuracy, energy consumption, time-to-train, inference latency, model size, total cost of training and more. One commonly-used proxy for the *efficiency* is the total number of floating-point operations (FLOPs) used. However, there is often a significant disparity between the efficiency one would expect from the FLOP count (which we describe as the *theoretical efficiency*) and the observed performance on modern hardware accelerators. This disparity holds especially for training (Touvron

<sup>\*</sup>Equal contribution <sup>1</sup>Graphcore Research, Bristol, UK  
<sup>2</sup>Graphcore Research, London, UK. Correspondence to: Dominic Masters <dominicm@graphcore.ai>.

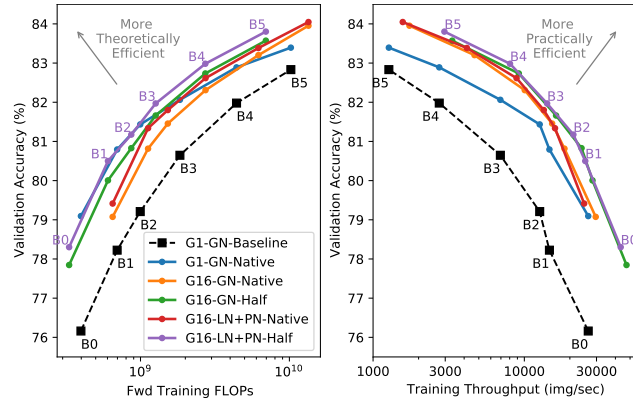


Figure 1. Theoretical (left) and practical (right) training efficiency of EfficientNet B0-B5 models using our three proposed improvements: (i) group convolutions [G16 (ours) vs G1]; (ii) proxy-normalized activations [LN+PN (ours) vs GN] and (iii) half-resolution training [Half (ours) vs Native]. Results show the best accuracy achieved when fine-tuning and testing on a range of resolutions. Baseline has no fine-tuning and uses the *native* image resolution.

et al., 2021; Lee et al., 2020). One reason for this is that not all FLOPs are created equal: optimising the FLOP count can often have the side effect of requiring additional data movement or poorly utilising vectorised hardware instructions. This can adversely affect the total FLOP rate. In this work, we aim to improve the *practical efficiency* of EfficientNet B0-B5, which were originally optimised for FLOPs, and better realise their promise as low-resource, high-performing networks. To this end, we consider three algorithmic improvements to EfficientNet:

- Generalising depthwise convolutions to group convolutions;
- Applying *proxy-normalized activations* to bridge the performance gap between batch-independent normalization methods and Batch Normalization;
- Reducing compute by lowering the training resolution and inexpensively fine-tuning at higher resolution.

We find that all three methods improve training accuracy and/or throughput such that their combination increases

training and inference throughput by up to  $7\times$  and  $3.6\times$ , respectively, and reduces inference latency by up to  $1.4\times$ .

## 2. Background

### 2.1. Efficient CNNs

Practical training efficiency improvements have been a significant enabler of innovation throughout the evolution of CNNs. For example, the innovation of AlexNet (Krizhevsky et al., 2012) was largely enabled due to GPU acceleration, and arguably, the success of ResNet (He et al., 2015) can be attributed not just to its good task performance but also due to its high throughput on GPUs relative to alternative models.

More recently, major improvements in terms of theoretical efficiency have been achieved. The most notable innovation has been the introduction of group and depthwise convolutions for spatial operations. Introducing group convolutions alone was found to improve the theoretical efficiency of ResNet-50 (Xie et al., 2016; Ioannou et al., 2016). Similarly, by reducing the group size to 1, Chollet (2016) leveraged depthwise convolutions to achieve gains in theoretical efficiency with respect to analogous models with dense convolutions. In particular, this led to major advances in compute- and memory-constrained “mobile” applications (Howard et al., 2017; Zhang et al., 2017b; Iandola et al., 2016; Sandler et al., 2018).

These theoretical efficiency benefits were further enhanced by directly minimising FLOPs using Neural Architecture Search (NAS). This led to efficiency improvements across the full spectrum of model sizes, from mobile-sized models like MobileNetV3 (Howard et al., 2019) and MNasNet (Tan et al., 2018) to large models like NASNet (Zoph et al., 2017) and AmoebaNet (Real et al., 2018). Notably, all NAS models that feature in the top-100 highest accuracy ImageNet models use group or depthwise convolutions in some form, further highlighting the advantage of these operations over their dense counterparts.<sup>1</sup> Building on the already efficient MNasNet, EfficientNet (Tan & Le, 2019) added improved training methods and scaling to much larger models to achieve SOTA performance across a broad spectrum of FLOP budgets.

While practical improvements were often achieved with “efficient” models for low power CPUs, these models have typically struggled to convert the theoretical gains into higher training throughput on high-performance hardware (Touvron et al., 2021; Lee et al., 2020). For example, while EfficientNets vastly outperform ResNets in terms of theoretical training efficiency, they have often been found to

underperform when considering practical training efficiency on GPUs (Lee et al., 2020). Some recent work has used NAS to optimise practical efficiency on GPUs (Cai et al., 2018; Vahdat et al., 2019; Lin et al., 2020). For the presented work, we prioritised hand-engineered solutions, but do not rule out NAS methods in future work.

### 2.2. Hardware Considerations

When investigating the practical efficiency of a model, it is important to understand the characteristics of the hardware it runs on. Discussion around this often focuses heavily on the peak compute rate, measured in floating-point operations per second (FLOPS), the theoretical maximum rate of compute operations. While the peak rate is an important factor to consider, it can be equally important to understand the assumptions required to achieve it – for example, the structure of the compute and the availability of data.

The compute structure is important as modern hardware typically utilises vector instructions that allow dot products of a given length to be computed with a single instruction. If, however, the compute cannot be structured such that these vector instructions are filled, FLOPs can potentially be wasted. Furthermore, if the data is not immediately available at the compute engine, then cycles will be required to move it. The extent to which this limitation manifests will be highly dependent on the *memory bandwidth*.

The reliance on memory bandwidth depends on the model and can be characterised by the ratio of compute to data transfer, i.e., the *arithmetic intensity* – where low arithmetic intensity operations are much more dependent on memory bandwidth. For a simple group convolution, arithmetic intensity monotonically increases with group size, kernel size, field size and batch size (see Appendix A). Notably, this means that the efficiency of depthwise convolutions and group convolutions with small group size is more likely to be limited by the available memory bandwidth.

In this work, we use a new class of hardware accelerator, the Graphcore IPU. This accelerator has many characteristics that set it aside from the GPUs that are commonly used for neural network training. The IPU compute is distributed across the chip in 1472 cores and, while its instructions are still vectorised, only dot products of 16 terms are required to utilise the compute engines fully. This helps to reduce the dependence on the compute structure. Furthermore, the IPU has over 900MB of high-bandwidth on-chip memory, significantly more than alternative hardware. This sharply reduces the cost of low arithmetic intensity operations.

To maximise performance on the IPU, it becomes important to keep as much of the working memory – for example, activation state – on-chip. This naturally promotes the use of much smaller batches, memory saving optimisation (Chen

<sup>1</sup><https://sotabench.com/benchmarks> accessed 4th February 2021

et al., 2016; Gruslys et al., 2016), and innovative forms of distributed processing (Harlap et al., 2018; Huang et al., 2019; Ben-Nun & Hoefer, 2018; Shazeer et al., 2018). At the same time, it does require reconsidering the use of Batch Normalization (Ioffe & Szegedy, 2015), the most common normalization method in vision models, which relies on large batches.

### 3. Methods

#### 3.1. Group Convolutions

As stated in Section 2.1, NAS methods tend to *group* their spatial convolutions, often with group size  $G = 1$  (depthwise convolutions). While depthwise convolutions are very FLOP and parameter efficient (Howard et al., 2017), using  $G > 1$  would utilise modern hardware accelerators more efficiently as a larger group size: (i) increases the arithmetic intensity (see Appendix A); (ii) increases the length of the dot products (used in the convolutions), allowing larger vector instructions to be utilised.

We aim to investigate the trade-offs involved in increasing the group size  $G$  of the spatial convolutions for the EfficientNet model. Increasing  $G$  alone would increase both parameter count and FLOPs. Therefore to maintain similar model complexity we correspondingly decreasing the *expansion ratio*, defined as the ratio of channels between the input to the first pointwise convolution and the spatial convolution. This is similar to the FLOP-equivalent scaling of the ResNeXt family (Xie et al., 2016). Therefore, a network with larger  $G$  will be *narrower* for the same FLOP count, yielding computational benefits by reducing the size of the stored activation state and facilitating the use of larger batch sizes. Note that while this compensation aims to keep the total FLOPs and parameters count similar to the baseline, for simplicity, we change the expansion ratio only at a global level. Consequently, we do not necessarily maintain the exact same distribution of parameters and FLOPs with depth.

As in EfficientNet, other NAS-derived architectures typically only use depthwise convolutions, which suggests that depthwise convolutions were optimal with respect to validation accuracy. In ResNeXts, increasing  $G$  while maintaining total FLOPs leads to decreasing validation accuracy. This would also suggest that vanilla EfficientNet, with  $G = 1$ , would achieve higher accuracy compared to similar networks with  $G > 1$ . Nevertheless, we hope that the modified networks offer better trade-offs between task performance and training time. We, therefore, test group sizes between  $G = 1$  and  $G = 64$  for EfficientNet B0 and B2.<sup>2</sup>

<sup>2</sup>For layers where the group size does not divide the channels, the group size is rounded to the nearest value that does.

#### 3.2. Batch-Independent Normalization

As mentioned in Section 2.2, vision models commonly rely on the use of Batch Normalization (BN) (Ioffe & Szegedy, 2015) to normalize activations throughout the network. BN is typically applied on the *unnormalized pre-activations*  $X$  to produce the *normalized pre-activations*  $Y$ , before an affine transform and a nonlinearity  $\phi$  finally produce the *post-activations*  $Z$ . Formally, for each channel  $c$ :

$$Y_{\dots c} = \frac{X_{\dots c} - \mu_c}{\sqrt{\sigma_c^2 + \epsilon}}, \quad (1)$$

$$Z_{\dots c} = \phi(\gamma_c Y_{\dots c} + \beta_c), \quad (2)$$

where  $\cdot$  is an index placeholder,  $\epsilon$  is BN’s numerical stability constant,  $\mu_c$ ,  $\sigma_c$  are the mean and standard deviation of  $X$  in channel  $c$ , and  $\gamma_c$ ,  $\beta_c$  are BN’s scale and shift parameters restoring in each channel  $c$  the two degrees of freedom lost in Eq. (1).

The normalization of BN in Eq. (1) ensures that  $Y$  is normalized, by which we mean that it has zero mean and unit variance in each channel  $c$ . This foundational principle of BN is essential for the successful scaling to large and deep models:

- (i) By ensuring that the nonlinearity  $\phi$  “sees” a data distribution close to normalized in each channel,<sup>3</sup>  $\phi$  can effectively be nonlinear *with respect to this distribution*. Consequently, additional layers can add expressive power and the network can effectively use its whole depth. This is opposed to a situation where  $\phi$  would “see” a “collapsed” data distribution, such that it would become well approximated at first order by a linear function with respect to this distribution;
- (ii) By ensuring that different channels have close to equal variance, the network can effectively use its whole width. This is opposite to a situation where a single channel would become arbitrarily dominant over the others, such that it would become the only channel “seen” by subsequent layers.

Despite the practical success deriving from this foundational principle, the reliance of BN on the mini-batch of data can sometimes be problematic. Most notably, when the mini-batch is small or when the dataset is large, the regularisation coming from the noise in the mini-batch statistics  $\mu_c$ ,  $\sigma_c$  can be excessive or unwanted, leading to degraded performance (Ioffe, 2017; Wu & He, 2018; Masters & Luschi, 2018;

<sup>3</sup>We say that a distribution is “close to normalized” when its mean is not far from zero and its variance not far from one. Since  $\gamma_c Y_{\dots c} + \beta_c$  and the normalized  $Y_{\dots c}$  are only separated by an affine transform with parameters not subject to weight decay, we implicitly assume that  $\gamma_c Y_{\dots c} + \beta_c$  is “close to normalized”.

Ying et al., 2018; Luo et al., 2018; Kolesnikov et al., 2020; Summers & Dinneen, 2020).

To circumvent these problems, a variety of batch-independent normalization techniques have been proposed in the literature: Layer Normalization (LN) (Ba et al., 2016), Group Normalization (GN) (Wu & He, 2018), Instance Normalization (IN) (Ulyanov et al., 2016), Weight Normalization (WN) (Salimans & Kingma, 2016), Weight Standardization (WS) (Qiao et al., 2019), Online Normalization (ON) (Chiley et al., 2019), Filter Response Normalization (FRN) (Singh & Krishnan, 2019), EvoNorm (Liu et al., 2020), being a non-exhaustive list. While useful in other contexts, none of these techniques managed to close the performance gap with large-batch BN in the context of this work, focused on EfficientNets trained with RMSProp on ImageNet.

This led us to rethink how to perform batch-independent normalization and, in concurrent work, propose *Proxy-Normalized Activations* (Labatie et al., 2021). In this work we formulate the postulate that, beyond lifting the reliance on the micro-batch, batch-independent normalization should also maintain BN’s principle of normalizing pre-activations  $Y$  in each channel. A first justification of this postulate is drawn from the benefits that are expected – as explained above – from this inductive bias of BN. A second justification is drawn, on a more practical level, from the fact that BN was used in architecture searches such as the one that yielded the EfficientNet family of models. Sticking to the same normalization principles might therefore spare the need of redoing these searches.

To retain BN’s principles while removing any dependence on the batch size, we extend the work of Arpit et al. (2016) as follows: (i) replacing the BN step of Eq. (1) by a batch-independent normalization step, based on either LN or GN; (ii) replacing the activation step of Eq. (2) by a *proxy-normalized activation* step. This step normalizes  $\phi(\gamma_c Y_{...c} + \beta_c)$  by assimilating it with  $\phi(\gamma_c \tilde{Y}_c + \beta_c)$ , where  $\tilde{Y}_c \sim \mathcal{N}(\tilde{\beta}_c, (1 + \tilde{\gamma}_c)^2)$  is a Gaussian *proxy* variable with mean  $\tilde{\beta}_c$  and variance  $(1 + \tilde{\gamma}_c)^2$  derived from the additional parameters  $\tilde{\beta}_c, \tilde{\gamma}_c$ .  $\tilde{\beta}_c, \tilde{\gamma}_c$  are subject to weight decay to express the prior that  $Y$  is close to normalized. If we choose LN as the batch-independent normalization, this is expressed for each batch element  $b$  and channel  $c$  as:

$$Y_{b...} = \frac{X_{b...} - \mu_b}{\sqrt{\sigma_b^2 + \epsilon}}, \quad (3)$$

$$Z_{...c} = \frac{\phi(\gamma_c Y_{...c} + \beta_c) - \mathbb{E}_{\tilde{Y}_c}[\phi(\gamma_c \tilde{Y}_c + \beta_c)]}{\sqrt{\text{Var}_{\tilde{Y}_c}[\phi(\gamma_c \tilde{Y}_c + \beta_c)] + \tilde{\epsilon}}}, \quad (4)$$

where  $\tilde{Y}_c \sim \mathcal{N}(\tilde{\beta}_c, (1 + \tilde{\gamma}_c)^2)$ ,  $\epsilon, \tilde{\epsilon}$  are respectively LN’s and proxy normalization’s numerical stability constants, and

$\mu_b, \sigma_b$  are the mean and standard deviation over the spatial and channel dimensions of the batch element  $b$  of  $X$ .

When combined with LN, such Proxy Normalization (PN) of activations iteratively ensures that pre-activations  $Y$  remain close to normalized. Indeed, when considering networks implementing Eq. (3) and Eq. (4) with random model parameters and large width, if pre-activations  $Y$  at some layer have their channels independent, Gaussian and normalized, then pre-activations at the next layer tend to have their channels normalized (see formal details in Appendix C).

### 3.3. Image Resolution

The introduction of global average pooling (Lin et al., 2013) allowed image classification CNNs to operate on inputs of arbitrary resolution. While this has been explored in tasks such as image segmentation (Long et al., 2014), in image classification, its impact is still to be fully understood. The EfficientNet model treats the image resolution as a tunable hyperparameter, using larger images to train larger networks. Hoffer et al. (2019) trained networks on several images sizes simultaneously, leading to either i) accelerated training to a target accuracy or ii) improved final performance for the same training resources. Perhaps closest to our aims, Howard (2018) recommends starting training with low-resolution images, increasing their size progressively during training, with the goal of reducing the total time-to-train.

In recent works, Touvron et al. (2019; 2020) showed that small amounts of fine-tuning can enable a network to process test images at higher resolution than during training. The fine-tuning step only needs to act on the final portion of the network, and only for a few epochs, to increase the overall accuracy. Consequently, the computational cost of fine-tuning is almost negligible in comparison to the rest of training.

We take inspiration from this to investigate fine-tuning of a network trained on low-resolution images and generalising it to larger resolutions for the perspective of efficiency. The use of smaller images during training allows us to train a given model faster, using less memory, or to train a larger model in the same amount of time. To test this idea, we compare training at the native EfficientNet image size (as defined in Tan & Le (2019) – reproduced in Table 1) to training with approximately half the original number of pixels (width and height therefore approximately  $1/\sqrt{2}$  times the original), which we denote as *half resolution*. In particular, this approximately matches the FLOPs of the EfficientNet model one size down.

We then fine-tune and test at a range of image sizes up to  $700 \times 700$ . When choosing the precise resolution to use for validation, we note that performance can suffer from an

aliasing artefact. This artefact arises due to the locations of asymmetric downsampling layers, where the input field dimensions are odd, which happens at different depths depending on the input resolutions. We find that it is important to keep the location of these downsampling layers consistent between training and testing. This can be achieved by choosing the test resolution,  $r_{test}$ , such that  $r_{train} \equiv r_{test} \pmod{2^n}$  where  $n$  is the number of downsampling layers in the model ( $n = 5$  for EfficientNet).

We also choose our *half resolution* to approximately halve the total number of pixels from the original EfficientNet training resolutions (Tan & Le, 2019), while satisfying this condition (see Table 1). This allows for direct comparisons to be made between the two training regimes.

Table 1. Image sizes used for training in native and half resolution.

	B0	B1	B2	B3	B4	B5
NATIVE	224	240	260	300	380	456
HALF	160	176	192	204	252	328

### 3.4. Implementation Details

Throughout this work, unless otherwise stated, we run our experiments on a Graphcore POD16 server. This contains  $4 \times$  M2000s, that have each  $4 \times$  MK2 IPU chips along with  $2 \times$  AMD EPYC 7742 64-core CPUs. Each IPU chip has 1472 cores, with 642KB of local SRAM for each core, totalling in excess of 900MB of high-bandwidth on-chip memory. Further storage is provided by off-chip DDR4. The results are generated using the TensorFlow (Abadi et al., 2015) framework with Poplar SDK v2.0<sup>4</sup>

During training, the model is divided into several *stages* that are processed in a pipeline across 2 or 4 chips, to maximise IPU utilisation. Following the pipelined paradigm, we do not process an entire mini-batch simultaneously. Instead, we sequentially compute and accumulate gradients for many smaller *micro-batches*, before applying the weight update with global batch size  $B$ . Our model-parallel pipelined implementation reduces the memory requirements on each chip, allowing the use of larger micro-batches and thus increasing throughput. This scheme is similar to Huang et al. (2019), but differs from Harlap et al. (2018) in the detail that we recompute each forward stage before its respective backwards pass. We replicate this setup to use all available IPUs in a data-parallel configuration, allowing us to use all 16 IPUs. The arithmetic is computed in float-16 mixed-precision, with each weight’s optimiser state stored in float-32 (Micikevicius et al., 2017). For inference, a single IPU is used with all arithmetic operations and weights in float-16.

Our baseline EfficientNet model architecture is as described in Tan & Le (2019), except for the replacement of BN layers with GN with 4 groups (Wu & He, 2018). Thus, our training dynamics depend on the global mini-batch size but not the micro-batch size (unlike if we had used BN). We find that good task performance depends on the degree of regularisation we use. While the original EfficientNet paper uses AutoAugment (Cubuk et al., 2018), we find that the augmentation hyperparameters from the original work are not robust to small model modifications (see Table 6), which agrees with conclusions made in Brock et al. (2021a). Furthermore, AutoAugment is computationally costly and can make CPU performance the throughput bottleneck. We, therefore, follow the augmentation strategy of Brock et al. (2021a) by using a combination of Mixup (Zhang et al., 2017a) and CutMix (Yun et al., 2019). We find it beneficial to increase the strength of these methods as model size increases. Otherwise preprocessing steps follow the procedure of He et al. (2015).

The training procedure closely follows Tan & Le (2019). We train on ImageNet (Russakovsky et al., 2015) for 350 epochs with RMSProp (Tieleman & Hinton, 2012) and decay the learning rate exponentially by a factor 0.97 every 2.4 epochs. We use a weight decay of  $10^{-5}$  on the convolutional weights, a label smoothing factor of 0.1, and normalization and PN’s numerical stability constants  $\epsilon = 10^{-3}$  and  $\tilde{\epsilon} = 3 \times 10^{-2}$ . We use a slightly smaller global batch size  $B = 768$  across all training cases and scale the original learning rate and RMSProp decay factor. For the RMSprop optimiser we use learning rate  $B \times 2^{-14}$ , momentum 0.9 and decay  $1.0 - B \times 2^{-14}$ . Our final weights are obtained by using an exponentially weighted average over checkpoints from each training epoch, with decay factor 0.97.

For fine-tuning we train, starting from the weight averaged checkpoint, for an additional 2 epochs, using vanilla Stochastic Gradient Descent (SGD) with a global batch size  $B = 512$ . We use a cosine learning rate schedule with an initial learning rate of 0.25 and the same preprocessing as for validation, as suggested in Touvron et al. (2019). We consider three different depths to fine-tune from: (i) the *last block* which contains the final convolution, normalization and fully connected layer weights; (ii) the *last two blocks* which also include all weights up to and including the previous downsampling layer; or (iii), the *last three blocks* which contain all weights back one further downsampling layer. This was done to keep the *proportion* of layers that are fine-tuned approximately independent of the model size.

All our accuracy results derive from an averaging over three independent runs. Real data is used for all training throughput measurements. For inference cases, we use synthetic data as a real production inference pipeline would differ from the setup we use in this work, which primarily aims to

<sup>4</sup><https://www.graphcore.ai/products/poplar>

calculate validation accuracy.

## 4. Results

### 4.1. Group Convolutions

In Table 2, we present the results of our experiments for different group and network sizes. We use EfficientNet B0 and B2 as a test-bed and sweep a range of group sizes. The experiments show that the validation performance for  $G \in \{4, 16\}$  matches or exceeds the vanilla baseline performance.

While the group size  $G = 4$  case achieves the best overall validation accuracy in these tests, we find that the increased computational benefits of group size  $G = 16$  yields a superior trade-off in practice. We refer to this model as *G16-EfficientNet*. We leave further investigation of the *G4-EfficientNet* to future work.

Testing the *G16-EfficientNet* for EfficientNet B1, B3, B4 and B5 (Table 2), we find that the validation accuracy is actually higher for  $G = 16$  than for the  $G = 1$  baseline. This result exceeds our expectations and suggests that this variant is not only faster but also more accurate. When testing on the full range of image sizes, we see further performance improvements for *G16-EfficientNet* over the group size  $G = 1$  baseline (Table 4-5, Figure 3a).

Table 2. Validation accuracy  $\pm$  standard deviation (%) for different group sizes. All training and validation experiments performed at the native image size, with Group Normalization and without fine-tuning.

SIZE	G	E	P	F	ACCURACY
B0	1	6	5.3	0.4	76.2 $\pm$ 0.1
	4	5	5.1	0.4	76.4 $\pm$ 0.1
	16	4	5.9	0.6	76.2 $\pm$ 0.3
	32	3	6.2	0.9	75.4 $\pm$ 0.1
	64	2	6.7	1.5	73.9 $\pm$ 0.1
B1	1	6	7.8	0.7	78.2 $\pm$ 0.1
	16	4	8.3	1.1	78.3 $\pm$ 0.1
B2	1	6	9.1	1.0	79.2 $\pm$ 0.2
	4	5	8.6	1.0	79.7 $\pm$ 0.1
	16	4	9.5	1.5	79.4 $\pm$ 0.1
	32	3	10.3	2.1	78.5 $\pm$ 0.2
	64	2	9.9	3.6	76.9 $\pm$ 0.1
B3	1	6	12.2	1.8	80.6 $\pm$ 0.0
	16	4	12.6	2.7	80.9 $\pm$ 0.1
B4	1	6	19.3	4.4	82.0 $\pm$ 0.0
	16	4	19.3	6.2	82.3 $\pm$ 0.1
B5	1	6	30.4	10.2	82.8 $\pm$ 0.1
	16	4	28.7	13.4	83.4 $\pm$ 0.1

\* G = group size, E = expansion ratio,  
P = parameters (millions), F = FLOPs (billions)

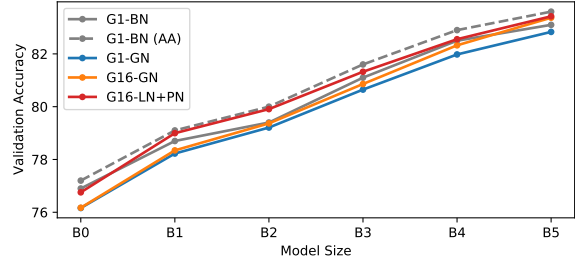


Figure 2. Validation accuracy with Group Normalization (GN) and Layer Normalization + Proxy-Normalized Activations (LN+PN) compared with Batch Normalization (BN) for different model sizes.

### 4.2. Proxy-Normalized Activations

Table 3 and Figure 2 show that accuracy results obtained with LN+PN match accuracy results obtained with BN across all model sizes. This conclusion holds if we assume that: (i) our regularisation strategy is an “intermediate” between the baseline preprocessing and the computationally expensive AutoAugment; (ii) accuracy results with BN are similar in the  $G = 1$  and  $G = 16$  cases. In any case, Table 3 shows that the accuracy achieved with LN+PN matches the best accuracy obtained with BN when directly comparing the two methods on  $G = 16$  for both B0 and B2.

Beyond the theoretical considerations of Section 3.2, the choice of combining LN with PN is thus backed by experimental results.

### 4.3. Train-Test Image Resolution

Figure 3 shows the effects of fine-tuning and testing across the full sweep of validation image sizes for EfficientNet-B3. Fine-tuning is shown to improve all networks’ accuracies. However, as we increase the number of fine-tuned layers, improvements in validation accuracy mainly occur at large image resolution. This supports the intuition that the further we get from the training distribution, the more layers we need to fine-tune. Although the best validation accuracies are seen at high resolution, it may be practical to accept a slight degradation of performance in return for the reduced cost of inference at lower resolutions.

Interestingly, we see different fine-tuning characteristics for the G1- and G16-EfficientNet models in Figure 3a. With little or no fine-tuning, the G16 model performs significantly better at large image resolutions. While this performance gap is largely eliminated as more layers get fine-tuned, it may again suggest that the G16 model has beneficial generalisation properties compared to the vanilla G1 model. In Figure 3c, we also see that the benefits provided by PN are robust across image sizes.

When comparing the different training resolutions in Fig-

Table 3. Comparison of validation accuracy  $\pm$  standard deviation (%) with Batch Normalization (BN), Group Normalization (GN) and Layer Normalization + Proxy-Normalized Activations (LN+PN). BN results show validation accuracy when training with baseline preprocessing and AutoAugment, respectively. BN results generally reproduced from (Tan et al., 2018), with our BN results marked by \* (see Appendix B)

	$G = 1, E = 6$		$G = 16, E = 4$			
	BN	BN (AA)	BN	BN (AA)	GN	LN+PN
B0	76.9 $\pm$ 0.1*	77.2 $\pm$ 0.1*	76.8 $\pm$ 0.1*	76.7 $\pm$ 0.1*	76.2 $\pm$ 0.3	76.8 $\pm$ 0.1
B1	78.7	79.1	-	-	78.3 $\pm$ 0.1	79.0 $\pm$ 0.1
B2	79.4 $\pm$ 0.0*	80.0 $\pm$ 0.0*	79.5 $\pm$ 0.1*	79.7 $\pm$ 0.1*	79.4 $\pm$ 0.1	79.9 $\pm$ 0.1
B3	81.1	81.6	-	-	80.9 $\pm$ 0.1	81.3 $\pm$ 0.1
B4	82.5	82.9	-	-	82.3 $\pm$ 0.1	82.6 $\pm$ 0.1
B5	83.1	83.6	-	-	83.4 $\pm$ 0.1	83.4 $\pm$ 0.1

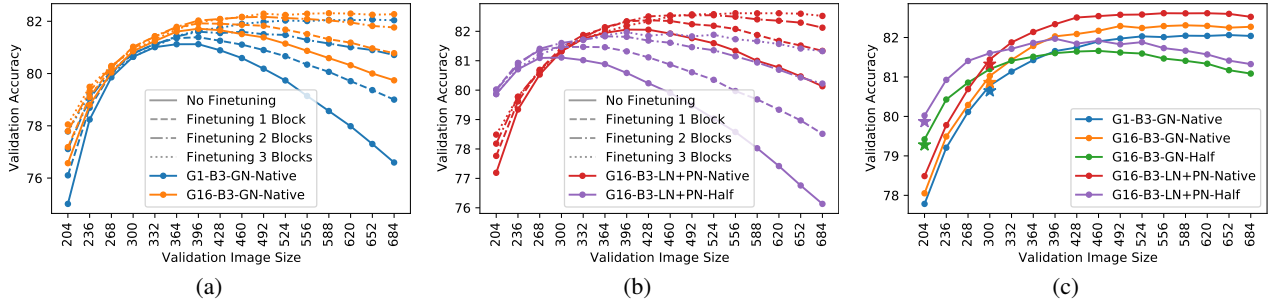


Figure 3. EfficientNet-B3 validation accuracy after fine-tuning for a range of fine-tuning/testing image sizes. (a)-(b) Effect of the number of fine-tuned blocks; (c) Results spanning different model and training configurations after fine-tuning with the optimal number of blocks. Label format G-M-R with G: group size, M: normalization method, R: training resolution.

ure 3b and Table 4, we surprisingly find that **models trained at half image size outperform models trained at native image size** when both are tested at native image size. We initially hypothesised that this could arise from the mismatch in the distribution of object sizes between the standard preprocessing of ImageNet at training and validation (Touvron et al., 2019). However, this difference was persistent even after fine-tuning the native-size training with validation preprocessing, suggesting that low-resolution training may itself offer a beneficial regularisation effect.

Comparing the different model sizes in Table 5, we see that, when testing at the *best* resolution, the highest accuracy is achieved by training at the larger, native image size. This, however, requires larger resolutions to be used in testing, which would adversely affect the inference cost.

This strongly suggests that we should *always* be fine-tuning and testing on larger images than trained on to achieve the best accuracy. Conversely, this also suggests that, to achieve maximum performance at a target test resolution, the model should be trained with smaller images. Half the size appears to be a reasonable choice, though a full sweep of training resolutions would be required to investigate whether this is indeed optimal. On the other hand, fine-tuning on lower

resolutions than trained on does not seem to offer any clear benefits.

#### 4.4. Training Efficiency

Figures 4 and 5 present the results of Tables 4 and 5 from the perspective of efficiency. Primarily, we see that there are clear efficiency benefits to training at half resolution. In the context of native resolution testing (Figure 4 and Table 4), we see that the  $2\times$  improvement in theoretical efficiency is directly reflected in terms of practical throughput. When testing with the *best* image resolution (Figure 5 and Table 5), the gap between the training resolutions is decreased significantly, suggesting that the increased ratio of test to training resolution is a significant factor.

For the G1-EfficientNet case, we see a much worse translation of theoretical efficiency to practical gains compared to G16-EfficientNet. This strongly supports the choice of adopting group convolutions.

For the LN+PN configurations, we see theoretical efficiency benefits due to the increased accuracy over the corresponding models with GN. In practice, however, we find that the efficiency curves are not substantially improved due to ap-

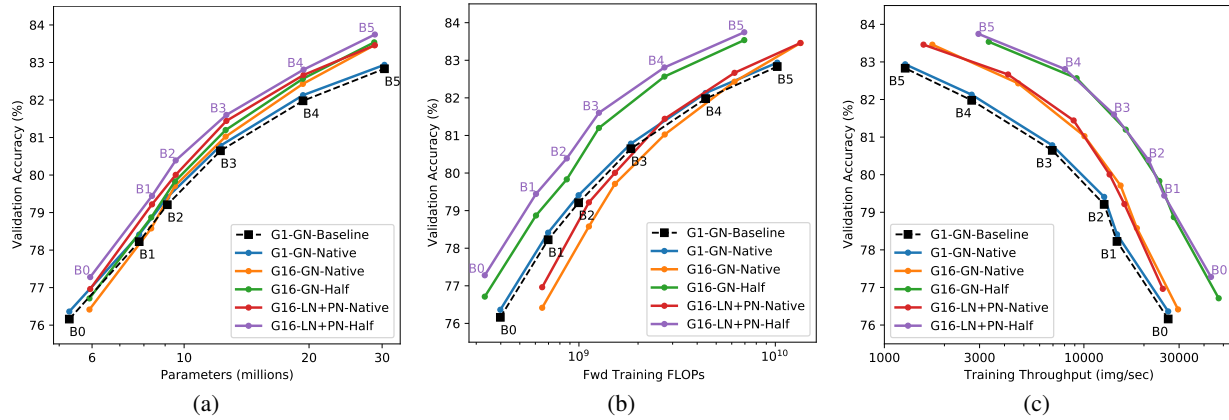


Figure 4. Comparison of parameter (a), theoretical (b) and practical (c) efficiency when fine-tuning and testing at the **native image resolution**. Label format defined as G-M-R for G: group size, M: normalization method, R: training resolution. G1-GN-Baseline case uses native resolution but is not fine-tuned.

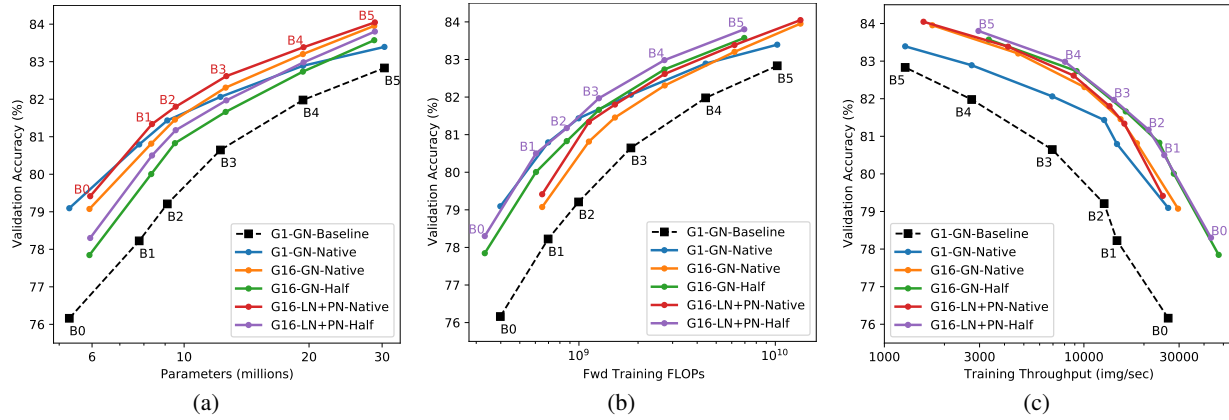


Figure 5. Comparison of parameter (a), theoretical (b) and practical (c) efficiency when fine-tuning and testing at the **best image resolution**. Label format same as Figure 4.

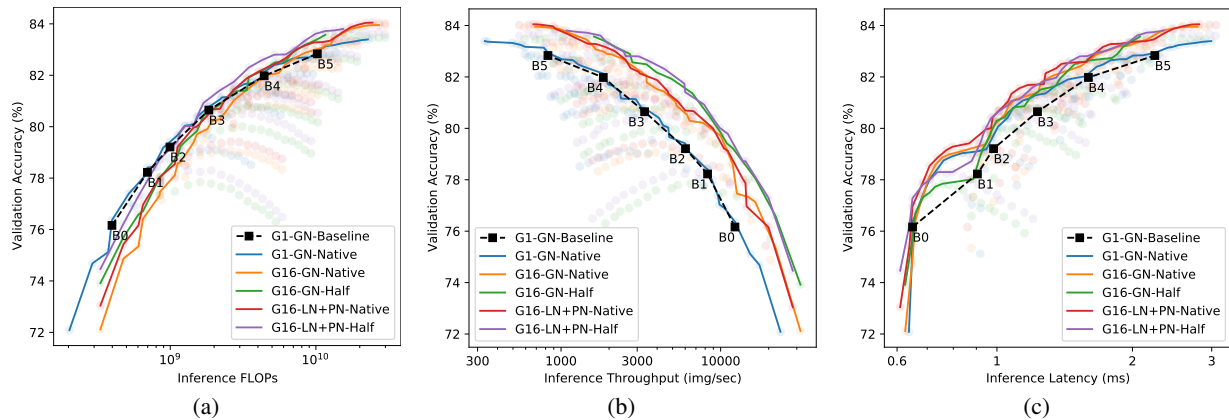


Figure 6. Comparison of theoretical inference efficiency (a) and two measures of practical inference efficiency: throughput at maximum batch size (b) and latency at batch size 1 (c). Points span different model sizes and different fine-tuning/testing resolutions; lines are Pareto fronts. Label format same as Figure 4.

Table 4. Validation accuracy  $\pm$  standard deviation (%) for different model sizes and training configurations, fine-tuned and tested at the **native image resolution**. Headers format defined as G-M-R for G: group size, M: normalization method, R: training resolution.

SIZE	G1-GN-NATIVE	G16-GN-NATIVE	G16-GN-HALF	G16-LN+PN-NATIVE	G16-LN+PN-HALF
B0	76.4 $\pm$ 0.1	76.4 $\pm$ 0.1	76.7 $\pm$ 0.2	77.0 $\pm$ 0.2	<b>77.3<math>\pm</math>0.1</b>
B1	78.4 $\pm$ 0.0	78.6 $\pm$ 0.1	78.9 $\pm$ 0.0	79.2 $\pm$ 0.1	<b>79.4<math>\pm</math>0.1</b>
B2	79.4 $\pm$ 0.2	79.7 $\pm$ 0.1	79.8 $\pm$ 0.1	80.0 $\pm$ 0.2	<b>80.4<math>\pm</math>0.1</b>
B3	80.8 $\pm$ 0.1	81.0 $\pm$ 0.1	81.2 $\pm$ 0.1	81.4 $\pm$ 0.2	<b>81.6<math>\pm</math>0.1</b>
B4	82.1 $\pm$ 0.1	82.4 $\pm$ 0.1	82.6 $\pm$ 0.1	82.7 $\pm$ 0.1	<b>82.8<math>\pm</math>0.1</b>
B5	82.9 $\pm$ 0.1	83.5 $\pm$ 0.1	83.5 $\pm$ 0.1	83.5 $\pm$ 0.1	<b>83.8<math>\pm</math>0.1</b>

Table 5. Validation accuracy  $\pm$  standard deviation (%) for different model sizes and training configurations, fine-tuned and tested at the **best image resolution**. Best resolution shown in [ ]. Headers as described above.

SIZE	G1-GN-NATIVE	G16-GN-NATIVE	G16-GN-HALF	G16-LN+PN-NATIVE	G16-LN+PN-HALF
B0	79.1 $\pm$ 0.2 [480]	79.1 $\pm$ 0.1 [416]	77.8 $\pm$ 0.1 [352]	<b>79.4<math>\pm</math>0.0 [448]</b>	78.3 $\pm$ 0.1 [384]
B1	80.8 $\pm$ 0.2 [528]	80.8 $\pm$ 0.0 [528]	80.0 $\pm$ 0.1 [400]	<b>81.3<math>\pm</math>0.1 [528]</b>	80.5 $\pm$ 0.1 [400]
B2	81.4 $\pm$ 0.1 [548]	81.5 $\pm$ 0.1 [516]	80.8 $\pm$ 0.1 [388]	<b>81.8<math>\pm</math>0.1 [516]</b>	81.2 $\pm$ 0.0 [420]
B3	82.1 $\pm$ 0.0 [652]	82.3 $\pm$ 0.1 [588]	81.7 $\pm$ 0.0 [460]	<b>82.6<math>\pm</math>0.0 [556]</b>	82.0 $\pm$ 0.1 [396]
B4	82.9 $\pm$ 0.1 [668]	83.2 $\pm$ 0.1 [572]	82.7 $\pm$ 0.1 [508]	<b>83.4<math>\pm</math>0.1 [604]</b>	83.0 $\pm$ 0.1 [444]
B5	83.4 $\pm$ 0.1 [680]	84.0 $\pm$ 0.1 [648]	83.6 $\pm$ 0.1 [424]	<b>84.0<math>\pm</math>0.1 [616]</b>	83.8 $\pm$ 0.0 [488]

proximately a 10% throughput cost. Importantly we do see a benefit in the number of parameters used in these cases and hope that the theoretical efficiency gains can be realised in practice with further software optimisation.

For the most efficient LN+PN-Half configuration, tested at the best image resolution, we see a  $3\times$  to  $7\times$  increase in training throughput compared to the non-fine-tuned baseline.

#### 4.5. Inference Efficiency

Figure 6 presents efficiency results for inference, considering the maximum batch size throughput and batch size 1 for latency measurements. Here we see that half resolution training produces more theoretically efficient models for inference, due to better accuracy at smaller image size (see Figure 3). We also find that these Pareto optimal *Half* configurations still outperform the *Native* configurations for training throughput, highlighting that efficiency benefits can be achieved simultaneously in both training and inference with a single test resolution.

While this translates well to practical throughput efficiency at maximum batch size, for practical latency efficiency at batch size 1, the native training resolution cases fare better. In this case, larger image sizes are less strongly penalised, since increased memory cost does not result in the use of a lower batch size.

The G1-EfficientNet variant again does not manage to convert the theoretical efficiency gains into practical throughput gains as well as the G16 variant. G1 does, however, perform comparably for the minimum latency case. Similarly to the

large image size case, this suggests that this variant benefits from lower penalisation of large memory costs.

Across both practical cases, the G16-LN+PN models improve efficiency over the baseline models, achieving a  $1.9\times$  to  $3.6\times$  throughput increase and up to  $1.4\times$  latency improvement.

## 5. Conclusion

We have proposed three distinct, complementary techniques for improving the practical efficiency of EfficientNet models. Based on a broad set of experimental results, each of these techniques has been shown to provide improved validation accuracy for the same computational cost and/or equivalent accuracy at reduced training cost. When using all three methods in combination, we achieved throughput benefits of up  $7\times$  and  $3.6\times$  compared to the baseline at the same validation accuracy.

## 6. Concurrent Work

Some concurrent work has drawn similar conclusions to those we present here.

Tan & Le (2021) also investigated how to speed up EfficientNet in practice. In agreement with this work they found that training on lower resolution images provided significant gains in practical efficiency. However they chose to progressively increase the resolution throughout training rather than finetune it at the end. They also modified the model itself, and in similar fashion to this work, chose to “densify” the MBconv blocks. They did this by replacing

the depthwise spatial convolution and the second pointwise convolution with a single dense, spatial convolution. They also found benefits from reducing the expansion factor to 4.

Brock et al. (2021b) looked at scaling up a ResNet-like model with batch independent normalization. They proposed a new approach to normalization based on weight standardization (Qiao et al., 2019) and layerwise scaling. However, based on Brock et al. (2021a); Labat et al. (2021) we believe this approach would not be effective on EfficientNet. They also highlighted that training on smaller images than the original EfficientNet work was key to achieving good training efficiency. Bello et al. (2021) also showed strong evidence to support the benefits of using lower resolution images in training.

## References

Abadi, M., Agarwal, A., Barham, P., Brevdo, E., Chen, Z., Citro, C., Corrado, G. S., Davis, A., Dean, J., Devin, M., Ghemawat, S., Goodfellow, I., Harp, A., Irving, G., Isard, M., Jia, Y., Jozefowicz, R., Kaiser, L., Kudlur, M., Levenberg, J., Mané, D., Monga, R., Moore, S., Murray, D., Olah, C., Schuster, M., Shlens, J., Steiner, B., Sutskever, I., Talwar, K., Tucker, P., Vanhoucke, V., Vasudevan, V., Viégas, F., Vinyals, O., Warden, P., Wattenberg, M., Wicke, M., Yu, Y., and Zheng, X. TensorFlow: Large-scale machine learning on heterogeneous systems, 2015. URL <https://www.tensorflow.org/>. Software available from tensorflow.org.

Arpit, D., Zhou, Y., Kota, B. U., and Govindaraju, V. Normalization propagation: A parametric technique for removing internal covariate shift in deep networks. *arXiv preprint arXiv:1603.01431 [stat.ML]*, 2016.

Ba, J. L., Kiros, J. R., and Hinton, G. E. Layer normalization. *arXiv preprint arXiv:1607.06450 [stat.ML]*, 2016.

Bello, I., Fedus, W., Du, X., Cubuk, E. D., Srinivas, A., Lin, T.-Y., Shlens, J., and Zoph, B. Revisiting resnets: Improved training and scaling strategies. *arXiv preprint arXiv:2103.07579*, 2021.

Ben-Nun, T. and Hoefler, T. Demystifying parallel and distributed deep learning: An in-depth concurrency analysis. *arXiv preprint arXiv:1802.09941 [cs.LG]*, 2018.

Brock, A., De, S., and Smith, S. L. Characterizing signal propagation to close the performance gap in unnormalized ResNets. *arXiv preprint arXiv:2101.08692 [cs.LG]*, 2021a.

Brock, A., De, S., Smith, S. L., and Simonyan, K. High-performance large-scale image recognition without normalization. *arXiv preprint arXiv:2102.06171*, 2021b.

Cai, H., Zhu, L., and Han, S. ProxylessNAS: Direct neural architecture search on target task and hardware. *arXiv preprint arXiv:1812.00332 [cs.LG]*, 2018.

Chen, T., Xu, B., Zhang, C., and Guestrin, C. Training deep nets with sublinear memory cost. *arXiv preprint arXiv:1604.06174 [cs.LG]*, 2016.

Chiley, V., Sharapov, I., Kosson, a., Koster, U., Reece, R., Samaniego de la Fuente, S., Subbiah, V., and James, M. Online normalization for training neural networks. *arXiv preprint arXiv:1905.05894 [cs.LG]*, 2019.

Chollet, F. Xception: Deep learning with depthwise separable convolutions. *arXiv preprint arXiv:1610.02357 [cs.CV]*, 2016.

Cubuk, E. D., Zoph, B., Mane, D., Vasudevan, V., and Le, Q. V. AutoAugment: Learning augmentation policies from data. *arXiv preprint arXiv:1805.09501 [cs.CV]*, 2018.

Gruslys, A., Munos, R., Danihelka, I., and Graves, A. Memory-efficient backpropagation through time. *arXiv preprint arXiv:1606.03401 [cs.NE]*, 2016.

Harlap, A., Narayanan, D., Phanishayee, A., Seshadri, V., devanur, N., Ganger, G., and Gibbons, P. PipeDream: Fast and efficient pipeline parallel DNN training. *arXiv preprint arXiv:1806.03377 [cs.DC]*, 2018.

He, K., Zhang, X., Ren, S., and Sun, J. Deep residual learning for image recognition. *arXiv preprint arXiv:1512.03385 [cs.CV]*, 2015.

Hoffer, E., Weinstein, B., Hubara, I., Ben-Nun, T., Hoefler, T., and Soudry, D. Mix & Match: Training convnets with mixed image sizes for improved accuracy, speed and scale resiliency. *arXiv preprint arXiv:1908.08986 [cs.CV]*, 2019.

Howard, A., Sandler, M., Chu, G., Chen, L.-C., Chen, B., Tan, M., Wang, W., Zhu, Y., Pang, R., Vasudevan, V., Le, Q. V., and Adam, H. Searching for MobileNetV3. *arXiv preprint arXiv:1905.02244 [cs.CV]*, 2019.

Howard, A. G., Zhu, M., Bo, C., Kalinichenko, D., Wang, W., Weyand, T., Andreetto, M., and Adam, H. MobileNets: Efficient convolutional neural networks for mobile vision applications. *arXiv preprint arXiv:1704.04861 [cs.CV]*, 2017.

Howard, J. Training Imagenet in 3 hours for \$25; and CIFAR10 for \$0.26. *Fast AI*, 2018. URL <https://www.fast.ai/2018/04/30/dawnbench-fastai/>.

Huang, Y., Cheng, Y., Bapna, A., Firat, O., Chen, M. X., Chen, D., Lee, H., Ngiam, J., Le, Q. V., Wu, Y., and

Chen, Z. GPipe: Efficient training of giant neural networks using pipeline parallelism. *arXiv preprint arXiv:1811.06965 [cs.CV]*, 2019.

Iandola, F. N., Han, S., Moskewicz, M. W., Ashraf, K., Dally, W. J., and Keutzer, K. SqueezeNet: AlexNet-level accuracy with  $50\times$  fewer parameters and  $<0.5\text{MB}$  model size. *arXiv preprint arXiv:1602.07360 [cs.CV]*, 2016.

Ioannou, Y., Robertson, D., Cipolla, R., and Criminisi, A. Deep Roots: Improving CNN efficiency with hierarchical filter groups. *arXiv preprint arXiv:1605.06489 [cs.NE]*, 2016.

Ioffe, S. Batch renormalization: Towards reducing mini-batch dependence in batch-normalized models. *arXiv preprint arXiv:1702.03275 [cs.LG]*, 2017.

Ioffe, S. and Szegedy, C. Batch normalization: Accelerating deep network training by reducing internal covariate shift. In *Proceedings of 32nd International Conference on Machine Learning, ICML 2015*, pp. 448–456, 2015.

Kolesnikov, A., Beyer, L., Zhai, X., Puigcerver, J., Yung, J., Gelly, S., and Houlsby, N. Big transfer (bit): General visual representation learning. In *Computer Vision - ECCV 2020 - 16th European Conference, Glasgow, UK, August 23-28, 2020, Proceedings, Part V*, volume 12350 of *Lecture Notes in Computer Science*, pp. 491–507. Springer, 2020.

Krizhevsky, A., Sutskever, I., and Hinton, G. E. ImageNet classification with deep convolutional neural networks. In *Advances in Neural Information Processing Systems 25, NIPS 2012*, 2012.

Labatie, A., Masters, D., Eaton-Rosen, Z., and Luschi, C. Proxy-normalizing activations to match batch normalization while removing batch dependence. *arXiv preprint arXiv:2106..*, 2021.

Lee, J., Won, T., Lee, T. K., Lee, H., Gu, G., and Hong, K. Compounding the performance improvements of assembled techniques in a convolutional neural network. *arXiv preprint arXiv:2001.06268 [cs.CV]*, 2020.

Lin, M., Chen, Q., and Yan, S. Network in network. *arXiv preprint arXiv:1312.4400 [cs.NE]*, 2013.

Lin, M., Chen, H., Sun, X., Qian, Q., Li, H., and Jin, R. Neural architecture design for GPU-efficient networks. *arXiv preprint arXiv:2006.14090 [cs.CV]*, 2020.

Liu, H., Brock, A., Simonyan, K., and Le, Q. V. Evolving normalization-activation layers. *arXiv preprint arXiv:2004.02967 [cs.LG]*, 2020.

Long, J., Shelhamer, and Darrel, T. Fully convolutional networks for semantic segmentation. *arXiv preprint arXiv:1411.4038 [cs.CV]*, 2014.

Luo, P., Wang, X., Shao, W., and Peng, Z. Towards understanding regularization in batch normalization. *arXiv preprint arXiv:1809.00846 [cs.LG]*, 2018.

Masters, D. and Luschi, C. Revisiting small batch training for deep neural networks. *arXiv preprint arXiv:1804.07612 [cs.LG]*, 2018.

Micikevicius, P., Narang, S., Alben, J., Diamos, G., Elen, E., Garcia, D., Ginsburg, B., Houston, M., Kichaeiv, O., Venkatesh, G., and Wu, H. Mixed precision training. *arXiv preprint arXiv:1710.03740 [cs.AI]*, 2017.

Qiao, S., Wang, H., Liu, C., Shen, W., and Yuille, A. Micro-batch training with batch-channel normalization and weight standardization. *arXiv preprint arXiv:1903.10520 [cs.CV]*, 2019.

Real, E., Aggarwal, A., Huang, Y., and Le, Q. V. Regularized evolution for image classifier architecture search. *arXiv preprint arXiv:1802.01548 [cs.NE]*, 2018.

Russakovsky, O., Deng, J., Su, H., Krause, J., Satheesh, S., Ma, S., Huang, Z., Karpathy, A., Khosla, A., Bernstein, M., Berg, A. C., and Fei-Fei, L. ImageNet large scale visual recognition challenge. *International Journal of Computer Vision (IJCV)*, 115(3):211–252, December 2015.

Salimans, T. and Kingma, D. P. Weight normalization: A simple reparameterization to accelerate training of deep neural networks. *arXiv preprint arXiv:1602.07868 [cs.LG]*, 2016.

Sandler, M., Howard, A., Zhu, M., Zhmoginov, A., and Chen, L.-C. MobileNetv2: Inverted residuals and linear bottlenecks. *arXiv preprint arXiv:1801.04381 [cs.CV]*, 2018.

Shazeer, N., Cheng, Y., Parmar, N., Tran, D., Vaswani, A., Koanantakool, P., Hawkins, P., Lee, H., Hong, M., Young, C., Sepassi, R., and Hechtman, B. MeshTensorFlow: Deep learning for supercomputers. *arXiv preprint arXiv:1811.02084 [cs.LG]*, 2018.

Singh, S. and Krishnan, S. Filter response normalization layer: Eliminating batch dependence in the training of deep neural networks. *arXiv preprint arXiv:1911.09737 [cs.LG]*, 2019.

Summers, C. and Dinneen, M. J. Four things everyone should know to improve batch normalization. In *8th International Conference on Learning Representations, ICLR 2020, Addis Ababa, Ethiopia, April 26-30, 2020. OpenReview.net*, 2020.

Tan, M. and Le, Q. V. EfficientNet: Rethinking model scaling for convolutional neural networks. *arXiv preprint arXiv:1905.11946 [cs.LG]*, 2019.

Tan, M. and Le, Q. V. EfficientNetV2: Smaller models and faster training. *arXiv preprint arXiv:2104.00298*, 2021.

Tan, M., Chen, B., Pang, R., Vasudevan, V., Sandler, M., Howard, A., and Le, Q. V. MnasNet: Platform-aware neural architecture search for mobile. *arXiv preprint arXiv:1807.11626 [cs.CV]*, 2018.

Tieleman, T. and Hinton, G. Lecture 6.5 - rmsprop. *COURSERA: Neural Networks for Machine Learning*, 2012.

Touvron, H., Vedaldi, A., Douze, M., and Jégou, H. Fixing the train-test resolution discrepancy. *arXiv preprint arXiv:1906.06423 [cs.CV]*, 2019.

Touvron, H., Vedaldi, A., Douze, M., and Jégou, H. Fixing the train-test resolution discrepancy: FixEfficientNet. *arXiv preprint arXiv:2003.08237 [cs.CV]*, 2020.

Touvron, H., Cord, M., Douze, M., Massa, F., Sablayrolles, A., and Jégou, H. Training data-efficient image transformers & distillation through attention, 2021.

Ulyanov, D., Vedaldi, A., and Lempitsky, V. Instance normalization: The missing ingredient for fast stylization. *arXiv preprint arXiv:1607.08022 [cs.CV]*, 2016.

Vahdat, A., Mallya, A., Liu, M.-Y., and Kautz, J. UNAS: Differentiable architecture search meets reinforcement learning. *arXiv preprint arXiv:1912.07651 [cs.LG]*, 2019.

Wu, T. and He, K. Group normalization. *arXiv preprint arXiv:1803.08494 [cs.CV]*, 2018.

Xie, S., Girshick, R., Dollár, P., Tu, Z., and He, K. Group normalization. *arXiv preprint arXiv:1611.05431 [cs.CV]*, 2016.

Ying, C., Kumar, S., Chen, D., Wang, T., and Cheng, Y. Image classification at supercomputer scale. *CoRR*, 2018.

Yun, S., Han, D., Oh, S. J., Chun, S., Choe, J., and Yoo, Y. CutMix: Regularization strategy to train strong classifiers with localizable features. *arXiv preprint arXiv:1905.04899 [cs.CV]*, 2019.

Zhang, H., Cissé, M., Dauphin, Y. N., and Lopez-Paz, D. mixup: Beyond empirical risk minimization. *arXiv preprint arXiv:1710.09412 [cs.LG]*, 2017a.

Zhang, X., Zhou, X., Lin, M., and Sun, J. ShuffleNet: An extremely efficient convolutional neural network for mobile devices. *arXiv preprint arXiv:1707.01083 [cs.CV]*, 2017b.

Zoph, B., Vasudevan, V., Shlens, J., and Le, Q. V. Learning transferable architectures for scalable image recognition. *arXiv preprint arXiv:1707.07012 [cs.CV]*, 2017.

## A. Arithmetic Intensity

One simple but useful metric when considering the practical performance of neural networks is the ratio of the compute (FLOPs) to memory transfer (bytes) required for the model. This dictates the memory bandwidth requirements of a hardware platform in order to ensure that the arithmetic compute units are sufficiently utilised.

Given the assumption that weight and activation state must always be transferred, we can compute the approximate intensity of an arbitrary convolution with batch size  $B$ , kernel size  $k \times k$ , field size  $f \times f$ , group size  $G$ , number of groups  $N$  and stride  $s$  as

$$I = \frac{\text{FLOPs}}{\text{Weight Mem} + \text{Act Mem}} \quad (5)$$

$$= \frac{G^2 k^2 B f^2 N / s}{k^2 G^2 N + B f^2 G N} \quad (6)$$

$$= \frac{G k^2 B f^2}{s(G k^2 + B f^2)} \quad (7)$$

From this we can see that arithmetic intensity has a positive monotonic relationship with  $G$ ,  $k$ ,  $b$  and  $f$  and a negative monotonic relationship with  $s$ . Interestingly the arithmetic intensity does not depend on the number of groups  $N$ .

## B. TPU Experiments

Machine learning experiments are often underspecified in the corresponding papers. To compare our models in the closest possible setting to the original “vanilla” EfficientNets, we used the public EfficientNet repository to run experiments using Google Cloud TPUs.<sup>5</sup> For these experiments, we ran EfficientNet experiments for B0 and B2, using the settings recommended in the repository. We also implemented and ran our G16 version of the network in this codebase. We ran each experiment (B0/B2; G1/G16) with and without “Autoaugment”, the recommended augmentation scheme.

The results of these experiments are presented in Table 6. For the cases without AutoAugment, the final performance of the “vanilla” networks is indistinguishable from the G16 versions. However, enabling AutoAugment appears to favour the “vanilla” networks. AutoAugment in general appears to be finely tuned – for instance, the AutoAugment parameters published in the public repository do not

<sup>5</sup><https://github.com/tensorflow/tpu/tree/master/models/official/efficientnet>, accessed 2020-13-12.

Table 6. Validation accuracy  $\pm$  standard deviation (%) for batch-normalized results on the TPU. For the “AutoAugment” cases, the AutoAugment hyperparameters were as specified in the code repository.

	Size	G1	G16
Baseline	B0	76.9 $\pm$ 0.06	76.8 $\pm$ 0.13
AutoAugment	B0	77.2 $\pm$ 0.09	76.7 $\pm$ 0.15
Baseline	B2	79.4 $\pm$ 0.04	79.5 $\pm$ 0.06
AutoAugment	B2	80.0 $\pm$ 0.03	79.7 $\pm$ 0.12

match the values published in Cubuk et al. (2018), suggesting that it has been re-tuned for G1 (vanilla) EfficientNets. Therefore, we would expect a similar tuning effort to yield augmentation parameters that would produce comparable results for our G16 networks.

## C. Iterative Guarantee of Normalization in Proxy-Normalized Networks

In this section, we slightly simplify our scope and adapt our notations.

We consider a fully-connected network without residual connections. Each layer  $l$  of this network is constituted of the succession of three steps: (i) matrix multiplication with weights  $\omega^l \in \mathbb{R}^{C_{l+1} \times C_l}$ , (ii) layer normalization, (iii) proxy-normalized activation with parameters  $\gamma^l$ ,  $\beta^l$  and  $\tilde{\gamma}^l$ ,  $\tilde{\beta}^l = 0$ .

We denote  $X^l$ ,  $Y^l$ ,  $Z^l$  the activations after each of these steps and we suppose that the set of batch elements  $b$  is countably infinite with  $X_b^l, Y_b^l, Z_b^l \in \mathbb{R}^{C_l}$  for each batch element  $b$ .

Note that our setup implicitly applies to convolutional networks having *only*  $1 \times 1$  convolutions and thus approximately to convolutional networks having *mostly*  $1 \times 1$  convolutions. Indeed, to move from the setup with only  $1 \times 1$  convolutions to our setup, it is sufficient to “merge” the batch and spatial dimensions in  $X^l$ ,  $Y^l$ ,  $Z^l$ .

We further use  $\mu$ ,  $\sigma$ ,  $\mathcal{P}$  indexed with a subset of components to denote the operators of mean, standard deviation and power of  $X^l$ ,  $Y^l$ ,  $Z^l$ , e.g.

$$\begin{aligned} \mu_b(Y^l) &= \mathbb{E}_c[Y_{bc}^l], & \mu_c(Y^l) &= \mathbb{E}_b[Y_{bc}^l], \\ \sigma_b(Y^l) &= \sqrt{\text{Var}_c[Y_{bc}^l]}, & \sigma_c(Y^l) &= \sqrt{\text{Var}_b[Y_{bc}^l]}, \\ \mathcal{P}_b(Y^l) &= \mathbb{E}_c[(Y_{bc}^l)^2], & \mathcal{P}_c(Y^l) &= \mathbb{E}_b[(Y_{bc}^l)^2]. \end{aligned}$$

We may now rewrite the three steps of layer  $l$  for each batch

element  $b$  and channel  $c$  as

$$\begin{aligned} X_b^l &= \omega^l Z_b^{l-1}, \\ Y_b^l &= \frac{X_b^l - \mu_b(X^l)}{\sigma_b(X^l)}, \\ Z_{\cdot c}^l &= \frac{\phi(\gamma_c^l Y_{\cdot c}^l + \beta_c^l) - \mathbb{E}_{\tilde{Y} \sim \mathcal{N}(0,1)}[\phi(\gamma_c^l \tilde{Y} + \beta_c^l)]}{\sqrt{\text{Var}_{\tilde{Y} \sim \mathcal{N}(0,1)}[\phi(\gamma_c^l \tilde{Y} + \beta_c^l)]}}, \end{aligned}$$

with the conventions that  $Z_b^0$  is the input of the network and that  $Y_b^l = 0$  when  $\sigma_b(X^l) = 0$  and  $Z_{\cdot c}^l = 0$  when  $\text{Var}_{\tilde{Y} \sim \mathcal{N}(0,1)}[\phi(\gamma_c^l \tilde{Y} + \beta_c^l)] = 0$ .

We denote  $\Theta^l = (\omega^l, \gamma^l, \beta^l, \dots, \omega^{l-1}, \gamma^{l-1}, \beta^{l-1}, \omega^l)$  and  $\theta^l = (\gamma^l, \beta^l, \omega^{l+1})$  and we suppose that  $\Theta^l$  is fixed and that  $\theta^l$  is random, with components of  $\gamma^l$ ,  $\beta^l$ ,  $\sqrt{C_l} \omega^{l+1}$  sampled *iid* from the fixed distributions  $\nu_\gamma$ ,  $\nu_\beta$ ,  $\nu_\omega$ .

We finally suppose that: (i) components of  $\gamma^l$  and  $\omega^l$  are almost surely nonzero, i.e.  $\nu_\gamma(\{0\}) = 0$ ,  $\nu_\omega(\{0\}) = 0$ ; (ii)  $\nu_\omega$  is symmetric around zero; (iii)  $\phi$  is such that there exists  $x$  with  $\phi(x) \neq 0$ .

**Assumption 1.**  $\Theta^l$  is chosen such that:

- $\forall c: Y_c^l$  is Gaussian and normalized with  $Y_c^l \sim \mathcal{N}(0, 1)$  w.r.t. the randomness coming from the batch element  $b$ ;
- $\forall (c, c')$  s.t.  $c \neq c'$ :  $Y_c^l$  and  $Y_{c'}^l$  are independent w.r.t. the randomness coming from the batch element  $b$ .

We proceed as follows:

1. We show (Theorem 1) that, under Assumption 1,  $\mu_b(X^{l+1})$ ,  $\sigma_b(X^{l+1})$  have a form of convergence in probability to respectively 0 and some  $\omega > 0$  as  $\min(C_l, C_{l+1}) \rightarrow \infty$ . This shows that  $Y_b^{l+1} = \frac{X_b^{l+1} - \mu_b(X^{l+1})}{\sigma_b(X^{l+1})}$  becomes well approximated by  $\frac{X_b^{l+1}}{\omega}$  as  $\min(C_l, C_{l+1}) \rightarrow \infty$ .
2. We show (Theorem 2) that, under Assumption 1,  $\frac{X_b^{l+1}}{\omega}$  becomes itself arbitrarily close to normalized as  $\min(C_l, C_{l+1}) \rightarrow \infty$ .

**Theorem 1.** For any  $1 > \eta > 0$  and  $\delta > 0$ , there exists  $\tilde{C}(\eta, \delta) \in \mathbb{N}^*$  such that if  $\min(C_l, C_{l+1}) \geq \tilde{C}(\eta, \delta)$ , it holds for any  $\Theta^l$  satisfying Assumption 1 that

$$\begin{aligned} \mathbb{P}_{b, \theta^l} \left[ |\mu_b(X^{l+1})| \leq \eta \right] &\geq 1 - \delta, \\ \mathbb{P}_{b, \theta^l} \left[ |\sigma_b(X^{l+1}) - \omega| \leq \eta \right] &\geq 1 - \delta, \end{aligned}$$

with  $\omega > 0$  the root mean square associated with  $\nu_\omega$ .

**Proof.** Let us fix  $\Theta^l$  satisfying Assumption 1.

For fixed  $c$ ,  $Z_{bc}^l$  has its distribution w.r.t. random  $b$  and random  $\gamma^l, \beta^l$  equal to the distribution of

$$\tilde{\phi}(Y, \gamma_c^l, \beta_c^l) \equiv \frac{\phi(\gamma_c^l Y + \beta_c^l) - \mathbb{E}_{\tilde{Y} \sim \mathcal{N}(0,1)}[\phi(\gamma_c^l \tilde{Y} + \beta_c^l)]}{\sqrt{\text{Var}_{\tilde{Y} \sim \mathcal{N}(0,1)}[\phi(\gamma_c^l \tilde{Y} + \beta_c^l)]}},$$

with  $Y \sim \mathcal{N}(0, 1)$  and  $\gamma_c^l \sim \nu_\gamma$  and  $\beta_c^l \sim \nu_\beta$ .

Furthermore, for fixed  $(c, c')$  s.t.  $c \neq c'$ , the assumption of independent  $Y_{bc}^l$  and  $Y_{bc'}^l$  w.r.t. random  $b$  combined with the assumption of iid components of  $\gamma^l$  and  $\beta^l$  implies that for any Borel sets  $I, J$ , the joint probability of the two events  $\{\tilde{\phi}(Y_{bc}^l, \gamma_c^l, \beta_c^l) \in I\}$  and  $\{\tilde{\phi}(Y_{bc'}^l, \gamma_{c'}^l, \beta_{c'}^l) \in J\}$  is equal to the product of the probability of the two events.

Thus, each channel  $c$  in  $Z_{bc}^l$  is iid w.r.t. random  $b$  and random  $\gamma^l, \beta^l$ .

Given  $\tilde{\phi}(Y_{bc}^l, \gamma_c^l, \beta_c^l) \sim \tilde{\phi}(Y_{b1}, \gamma_1^l, \beta_1^l)$  w.r.t.  $(b, \theta^l)$  for any  $c$ , it follows that

$$\begin{aligned} \mathbb{E}_{b, \theta^l}[\mathcal{P}_b(Z^l)] &= \mathbb{E}_{b, \gamma_1^l, \beta_1^l}[\tilde{\phi}(Y_{b1}, \gamma_1^l, \beta_1^l)^2] \\ &= \mathbb{E}_{\gamma_1^l \neq 0, \beta_1^l}[\mathbb{E}_b[\tilde{\phi}(Y_{b1}, \gamma_1^l, \beta_1^l)^2]] \quad (8) \\ &= \mathbb{E}_{\gamma_1^l \neq 0, \beta_1^l}[1] = 1, \\ \text{Var}_{b, \theta^l}[\mathcal{P}_b(Z^l)] &= \frac{1}{C_l} \text{Var}_{b, \gamma_1^l, \beta_1^l}[\tilde{\phi}(Y_{b1}, \gamma_1^l, \beta_1^l)^2] \\ &\equiv \frac{1}{C_l} V, \end{aligned}$$

with Eq. (8) obtained using  $\nu_\gamma(\{0\}) = 0$  and the assumption that there exists  $x$  with  $\phi(x) \neq 0$ , and with  $V$  a constant only depending on  $\nu_\gamma, \nu_\beta$ .

Chebyshev's inequality then gives for any  $\eta > 0$  that

$$\mathbb{P}_{b, \theta^l}[|\mathcal{P}_b(Z^l) - 1| \geq \eta] \leq \frac{1}{\eta^2 C_l} V. \quad (9)$$

Thus, for any  $1 > \eta > 0$  and  $\delta > 0$ , there exists  $C_1(\eta, \delta) \in \mathbb{N}^*$  independent of  $\Theta^l$  such that if  $C_l \geq C_1(\eta, \delta)$ , it holds with probability greater than  $1 - \delta$  w.r.t.  $(b, \theta^l)$  that

$$(1 - \eta) \leq \mathcal{P}_b(Z^l) \leq (1 + \eta). \quad (10)$$

Now, let us fix  $b$  as well as  $\Theta^l, \gamma^l, \beta^l$ . In that case,  $\mu_b(X^{l+1})$  and  $\mathcal{P}_b(X^{l+1})$  are obtained as a function of  $\omega^{l+1}$  as

$$\begin{aligned} \mu_b(X^{l+1}) &= \frac{1}{C_{l+1}} \sum_c \sum_{c'} \omega_{cc'}^{l+1} Z_{bc'}^l, \\ \mathcal{P}_b(X^{l+1}) &= \frac{1}{C_{l+1}} \sum_c \left( \sum_{c'} \omega_{cc'}^{l+1} Z_{bc'}^l \right)^2. \end{aligned}$$

Thus, the mean and variance of  $\mu_b(X^{l+1})$  w.r.t.  $\omega^{l+1}$  are given by

$$\begin{aligned} \mathbb{E}_{\omega^{l+1}}[\mu_b(X^{l+1})] &= 0, \quad (11) \\ \text{Var}_{\omega^{l+1}}[\mu_b(X^{l+1})] &= \frac{1}{C_{l+1}^2} \sum_c \sum_{c'} \text{Var}_{\omega^{l+1}}[\omega_{cc'}^{l+1} Z_{bc'}^l] \\ &= \frac{1}{C_{l+1}} \sum_{c'} \frac{1}{C_l} \omega^2 (Z_{bc'}^l)^2 \\ &= \frac{1}{C_{l+1}} \omega^2 \mathcal{P}_b(Z^l), \end{aligned}$$

where Eq. (11) is obtained by symmetry of  $\nu_\omega$  around zero and  $\omega$  is the root mean square associated with  $\nu_\omega$ .

Similarly, for the moments of  $\mathcal{P}_b(X^{l+1})$  w.r.t.  $\omega^{l+1}$ , we get

$$\begin{aligned} \mathbb{E}_{\omega^{l+1}}[\mathcal{P}_b(X^{l+1})] &= \frac{1}{C_{l+1}} \sum_c \sum_{c'} \frac{1}{C_l} \omega^2 (Z_{bc'}^l)^2, \\ &= \omega^2 \mathcal{P}_b(Z^l), \\ \text{Var}_{\omega^{l+1}}[\mathcal{P}_b(X^{l+1})] &= \frac{1}{C_{l+1}^2} \sum_c \text{Var}_{\omega^{l+1}} \left[ \left( \sum_{c'} \omega_{cc'}^{l+1} Z_{bc'}^l \right)^2 \right] \\ &= \frac{1}{C_{l+1}} \text{Var}_{\omega^{l+1}} \left[ \left( \sum_{c'} \omega_{1c'}^{l+1} Z_{bc'}^l \right)^2 \right] \\ &\leq \frac{1}{C_{l+1}} \mathbb{E}_{\omega^{l+1}} \left[ \left( \sum_{c'} \omega_{1c'}^{l+1} Z_{bc'}^l \right)^4 \right] \\ &\leq \frac{1}{C_{l+1}} \left( \sum_{c'} \mathbb{E}_{\omega^{l+1}}[(\omega_{1c'}^{l+1} Z_{bc'}^l)^4] \right. \\ &\quad \left. + 6 \sum_{c' < c''} \mathbb{E}_{\omega^{l+1}}[(\omega_{1c'}^{l+1} Z_{bc'}^l)^2] \mathbb{E}_{\omega^{l+1}}[(\omega_{1c''}^{l+1} Z_{bc''}^l)^2] \right), \end{aligned}$$

where we remind that  $\omega_{1c'}^{l+1} \sim \omega_{cc'}^{l+1}$  for any  $c, c'$ .

Using Cauchy-Schwarz inequality, we then get

$$\begin{aligned} \text{Var}_{\omega^{l+1}}[\mathcal{P}_b(X^{l+1})] &\leq \frac{1}{C_{l+1}} \left( \sum_{c'} \mathbb{E}_{\omega^{l+1}}[(\omega_{1c'}^{l+1})^4] (Z_{bc'}^l)^4 \right. \\ &\quad \left. + 3 \sum_{c' \neq c''} \mathbb{E}_{\omega^{l+1}}[(\omega_{1c'}^{l+1})^4] (Z_{bc'}^l)^2 (Z_{bc''}^l)^2 \right) \end{aligned}$$

In turn, this further gives

$$\begin{aligned}
 & \text{Var}_{\omega^{l+1}} [\mathcal{P}_b(X^{l+1})] \\
 & \leq \frac{1}{C_{l+1}} 3 \sum_{c', c''} \mathbb{E}_{\omega^{l+1}} \left[ (\omega_{1c'}^{l+1})^4 \right] (Z_{bc'}^l)^2 (Z_{bc''}^l)^2 \\
 & \leq \frac{1}{C_{l+1}} 3 \sum_{c', c''} \frac{1}{C_l^2} \tilde{\omega}^4 (Z_{bc'}^l)^2 (Z_{bc''}^l)^2 \\
 & \leq \frac{1}{C_{l+1}} 3 \tilde{\omega}^4 \mathcal{P}_b(Z^l)^2,
 \end{aligned} \tag{12}$$

where we defined  $\tilde{\omega} = \mathbb{E}_{\omega^{l+1}} \left[ (\sqrt{C_l} \omega_{11}^{l+1})^4 \right]^{1/4}$  the  $L^4$  norm of  $\sqrt{C_l} \omega_{11}^{l+1}$  having only a dependence in  $\nu_\omega$ .

Now let us define  $\hat{X}^{l+1}$  such that  $\hat{X}_{b \cdot}^{l+1} = \frac{1}{\omega \sqrt{\mathcal{P}_b(Z^l)}} X_{b \cdot}^{l+1}$  for any  $b$ , with the convention that  $\mu_b(\hat{X}^{l+1}) = 0$  and  $\mathcal{P}_b(\hat{X}^{l+1}) = 1$  when  $\mathcal{P}_b(Z^l) = 0$  (e.g. alternating between  $-1$  and  $+1$  values in  $\hat{X}^{l+1}$  if the number of channels is even).

We get for any  $b$  that

$$\begin{aligned}
 \mathbb{E}_{\omega^{l+1}} [\mu_b(\hat{X}^{l+1})] &= 0, \\
 \text{Var}_{\omega^{l+1}} [\mu_b(\hat{X}^{l+1})] &= \frac{1}{C_{l+1}}, \\
 \mathbb{E}_{\omega^{l+1}} [\mathcal{P}_b(\hat{X}^{l+1})] &= 1, \\
 \text{Var}_{\omega^{l+1}} [\mathcal{P}_b(\hat{X}^{l+1})] &\leq \frac{1}{C_{l+1}} 3 \tilde{\omega}^4 \omega^{-4}.
 \end{aligned}$$

In turn, this implies

$$\begin{aligned}
 \mathbb{E}_{b, \theta^l} [\mu_b(\hat{X}^{l+1})] &= 0, \\
 \text{Var}_{b, \theta^l} [\mu_b(\hat{X}^{l+1})] &= \frac{1}{C_{l+1}}, \\
 \mathbb{E}_{b, \theta^l} [\mathcal{P}_b(\hat{X}^{l+1})] &= 1, \\
 \text{Var}_{b, \theta^l} [\mathcal{P}_b(\hat{X}^{l+1})] &\leq \frac{1}{C_{l+1}} 3 \tilde{\omega}^4 \omega^{-4}.
 \end{aligned}$$

Using a reasoning similar to Eq. (9) and Eq. (10), it follows for any  $1 > \eta > 0$  and  $\delta > 0$  that there exists  $C_2(\eta, \delta) \in \mathbb{N}^*$  independent of  $\Theta^l$  such that if  $C_{l+1} \geq C_2(\eta, \delta)$ , it holds with probability greater than  $1 - \delta$  w.r.t.  $(b, \theta^l)$  that

$$\begin{aligned}
 & \left( -\eta \leq \mu_b(\hat{X}^{l+1}) \leq \eta \right) \\
 & \wedge \left( 1 - \eta \leq \mathcal{P}_b(\hat{X}^{l+1}) \leq 1 + \eta \right).
 \end{aligned} \tag{13}$$

Combining Eq. (10) and Eq. (13), we deduce for any  $1 > \eta > 0$  and  $\delta > 0$  that if  $\min(C_l, C_{l+1}) \geq$

$\min(C_1(\eta, \delta), C_2(\eta, \delta))$ , it holds with probability greater than  $1 - 2\delta$  w.r.t.  $(b, \theta^l)$  that

$$\begin{aligned}
 & \left( -\eta(1 + \eta)\omega \leq \mu_b(X^{l+1}) \leq \eta(1 + \eta)\omega \right) \\
 & \wedge \left( (1 - \eta)^2 \omega^2 \leq \mathcal{P}_b(X^{l+1}) \leq (1 + \eta)^2 \omega^2 \right).
 \end{aligned}$$

It follows for any  $1 > \eta > 0$  and  $\delta > 0$  that there exists  $\tilde{C}(\eta, \delta) \in \mathbb{N}^*$  independent of  $\Theta^l$  such that if  $C_{l+1} \geq \tilde{C}(\eta, \delta)$ , it holds with probability greater than  $1 - \delta$  w.r.t.  $(b, \theta^l)$  that

$$\left( |\mu_b(X^{l+1})| \leq \eta \right) \wedge \left( |\sigma_b(X^{l+1}) - \omega| \leq \eta \right).$$

This immediately gives the required result.  $\square$

**Theorem 2.** Fix a channel  $c$  at layer  $l + 1$  and define  $\check{Y}^{l+1} = \frac{X^{l+1}}{\omega}$ .

Then for any  $1 > \eta > 0$  and  $\delta > 0$ , there exists  $C(\eta, \delta) \in \mathbb{N}^*$  such that if  $C_l \geq C(\eta, \delta)$ , it holds for any  $\Theta^l$  satisfying Assumption 1 with probability greater than  $1 - \delta$  w.r.t.  $\theta^l$  that

$$\mu_c(\check{Y}^{l+1}) = 0, \quad |\sigma_c(\check{Y}^{l+1}) - 1| \leq \eta.$$

**Proof.** We start by noting that for any  $\Theta^l$  satisfying Assumption 1 and any  $c'$ , it holds a.s. w.r.t.  $\beta^l, \gamma^l$  that

$$\mu_{c'}(Z^l) = \mathbb{E}_b \left[ \tilde{\phi}(\gamma_{c'}^l Y_{bc'}^l + \beta_{c'}^l) \right] = 0, \tag{14}$$

$$\mathcal{P}_{c'}(Z^l) = \mathbb{E}_b \left[ \tilde{\phi}(\gamma_{c'}^l Y_{bc'}^l + \beta_{c'}^l)^2 \right] = 1, \tag{15}$$

$$\sigma_{c'}(Z^l) = 1, \tag{16}$$

where Eq. (15) follows from  $\nu_\gamma(\{0\}) = 0$  and the fact that there exists  $x$  such that  $\phi(x) \neq 0$ .

Thus, we get for any  $c$  that a.s. w.r.t.  $\beta^l, \gamma^l$ :

$$\begin{aligned}
 \mu_c(\check{Y}^{l+1}) &= \frac{1}{\omega} \sum_{c'} \omega_{cc'}^{l+1} \mu_{c'}(Z^l) \\
 &= 0, \\
 \sigma_c(\check{Y}^{l+1})^2 &= \frac{1}{\omega^2} \sum_{c'} (\omega_{cc'}^{l+1})^2 \sigma_{c'}(Z^l)^2 \\
 &= \frac{1}{\omega^2} \sum_{c'} (\omega_{cc'}^{l+1})^2, \\
 \mathcal{P}_c(\check{Y}^{l+1}) &= \frac{1}{\omega^2} \sum_{c'} (\omega_{cc'}^{l+1})^2,
 \end{aligned}$$

where we used Eq. (14) and Eq. (16) combined with the assumption of independent channels w.r.t.  $b$ .

The expectation and variance of  $\mathcal{P}_c(\check{Y}^{l+1})$  w.r.t.  $\theta^l$  are therefore such that

$$\begin{aligned}\mathbb{E}_{\theta^l} [\mathcal{P}_c(\check{Y}^{l+1})] &= 1, \\ \text{Var}_{\theta^l} [\mathcal{P}_c(\check{Y}^{l+1})] &= \frac{1}{\omega^2} \sum_{c'} \text{Var}_{\theta^l} [(\omega_{cc'}^{l+1})^2] \\ &\leq \frac{1}{\omega^2} \sum_{c'} \mathbb{E}_{\theta^l} [(\omega_{cc'}^{l+1})^4] \\ &\leq \frac{1}{\omega^2} \frac{1}{C_l} \tilde{\omega}^4,\end{aligned}$$

with  $\tilde{\omega}$  defined as in Eq. (12) as the  $L^4$  norm of  $\sqrt{C_l} \omega_{11}^{l+1}$  having only a dependence in  $\nu_\omega$ .

Using a reasoning similar to Eq. (9) and Eq. (10), it follows for any  $1 > \eta > 0$  and  $\delta > 0$  that there exists  $C_3(\eta, \delta) \in \mathbb{N}^*$  independent of  $\Theta^l$  such that if  $C_l \geq C_3(\eta, \delta)$ , it holds with probability greater than  $1 - \delta$  over  $\theta^l$  that

$$\mu_c(\check{Y}^{l+1}) = 0, \quad (17)$$

$$(\mathcal{P}_c(\check{Y}^{l+1}) - 1)^2 \leq \eta. \quad (18)$$

Next we note that if Eq. (17) and Eq. (18) hold, then

$$\begin{aligned}|\sigma_c(\check{Y}^{l+1}) - 1| &\leq |\sigma_c(\check{Y}^{l+1}) - 1| \cdot |\sigma_c(\check{Y}^{l+1}) + 1| \\ &\leq |\sigma_c(\check{Y}^{l+1})^2 - 1| \\ &\leq |\mathcal{P}_c(\check{Y}^{l+1}) - 1| \\ &\leq \sqrt{\eta}.\end{aligned}$$

Consequently, for any  $1 > \eta > 0$  and  $\delta > 0$  there exists  $C(\eta, \delta) \in \mathbb{N}^*$  independent of  $\Theta^l$  such that if  $C_l \geq C(\eta, \delta)$ , it holds with probability greater than  $1 - \delta$  over  $\theta^l$  that

$$\mu_c(\check{Y}^{l+1}) = 0, \quad |\sigma_c(\check{Y}^{l+1}) - 1| \leq \eta. \quad \square$$